Y. Cai
S. S. Chen
Argonne National Laboratory
9700 South Cass Avenue
Argonne, IL 60439

Numerical Analysis for Dynamic Instability of Electrodynamic Maglev Systems

Suspension instabilities in an electrodynamic maglev system with three- and five-degrees-of-freedom DOF vehicles traveling on a double L-shaped set of guideway conductors were investigated with various experimentally measured magnetic force data incorporated into theoretical models. Divergence and flutter were obtained from both analytical and numerical solutions for coupled vibration of the three-DOF maglev vehicle model. Instabilities of five direction motion (heave, slip, roll, pitch, and yaw) were observed for the five-DOF vehicle model. The results demonstrate that system parameters such as system damping, vehicle geometry, and coupling effects among five different motions play very important roles in the occurrence of dynamic instabilities of maglev vehicles. © *1995 John Wiley & Sons, Inc.**

INTRODUCTION

Because dynamic instabilities are not acceptable for any commercial maglev system, it is important to consider these phenomena when designing and developing maglev suspension systems (Cai et al., 1992a, 1992b, 1993a, 1993b). The objective of this study is to develop a general approach for investigating and predicting the occurrence of instabilities in maglev suspension systems and to provide a better understanding of the conditions (design features and parameter values) that can lead to dynamic instabilities.

The repulsive levitation system, or the so-called electrodynamic system (EDS), is often thought to be inherently stable. However, its response to perturbations is frequently unstable and susceptible to catastrophic oscillations, particularly in rectangular trough configurations. So far, only a few analytical and experimental studies (Cai et al., 1992a, 1992b) have been performed to understand the stability characteristics of EDS maglev systems. Davis and Wilkie (1971) studied a magnetic coil moving over a conducting track and concluded that negative damping occurs at velocities greater than the characteristic velocity based on thin-track theory. Ohno et al. (1973) studied the pulsating lift forces in a linear synchronous motor. These pulsating forces may cause parametric resonance and combination resonance, in addition to heave and pitch oscillations. Experiments on the MIT magneplane showed obvious evidence of dynamic instabilities on film in the early 1970s, but no detailed study

The submitted manuscript has been authored by a contractor of the US Government under contract No. W-31-109-ENG-38. *This article is a US Government work and, as such, is in the public domain in the United States of America.

Received February 17, 1994; Accepted March 7, 1995.

Shock and Vibration, Vol. 2, No. 4, pp. 339–349 (1995)

CCC 1070-9622/95/040339-11

was made of dynamic stability. An experimental vehicle with three degrees-of-freedom (DOF) floating above a large rotating wheel was found by Moon (1974) to have a lateral-roll-yaw instability. Also, experiments performed at MIT on a test track showed pitch-heave instability. Negative magnetic damping was demonstrated, but was dominated by aerodynamic damping (Moon, 1977). A conducting guideway, consisting of L-shaped aluminum segments attached to a rotating wheel to simulate the full-scale Japanese guideway at Miyazaki, was studied experimentally and analytically by Chu and Moon (1983). Divergence and flutter of a two-DOF vehicle model were obtained for coupled yaw-lateral vibration; the divergence leads to two stable equilibrium yaw positions, and the flutter instability leads to a limit cycle of coupled yaw and lateral motions in the neighborhood of the magnetic drag peak.

Because very limited studies have been published and many stability issues remain unresolved, the theory of motion-dependent magnetic-force-induced instability (which consists of both quasistatic motion and unsteady motion theories) was developed in our previous work (Cai et al., 1992a, 1992b, 1993a). The method of obtaining motion-dependent magnetic-force coefficients experimentally was identified, and quasistatic motion-dependent magnetic-force coefficients of a maglev system with a double L-shaped guideway were measured with this method, in an experimental investigation at Argonne National Laboratory (Cai et al., 1992b). Motion-dependent magnetic forces are the controlling elements in the stability of maglev systems. Therefore, this earlier integrated analytical/experimental study presented a systematic method on the stability of maglev systems and answered a series of questions on maglev stability. With a simplified three-DOF analytical vehicle model, divergence and flutter were observed for coupled vibration of vehicle on a guideway consisting of double L-shaped aluminum segments (Cai et al., 1992a, 1992b, 1993a).

Based on our previous study on dynamic stability problems of maglev systems, the focus of this study is on numerical analysis of dynamic instabilities of an EDS maglev suspension system with three- and five-DOF vehicles traveling on a double L-shaped set of guideway conductors. Both analytical and numerical approaches were used, and various magnetic suspension forces compiled from experimental data were incorporated into the theoretical models. Divergence and flutter were obtained from analytical and numerical solutions for coupled vibration of the three-DOF maglev vehicle model. A computer code for numerically simulating dynamic instability of the five-DOF vehicle model was developed, and extensive computations with various parameters were performed to understand the stability characteristics of EDS maglev systems. Instabilities of five direction motions (heave, slip, roll, pitch, and yaw) of the dynamic vehicle model were observed. This demonstrates that system parameters such as system damping, vehicle geometry, and coupling effects among five different motions play very important roles in the occurrence of dynamic instabilities in maglev systems.

SIMULATION FOR THREE-DOF MODEL

A three-DOF vehicle with the double L-shaped sheet guideway (Fig. 1) is considered in this study, to gain an understanding of stability characteristics. The vehicle can move vertically up and down the guideway (heave), move transversely to the guideway (slip), and it can rotate about the x axis, i.e., the direction of travel (roll). Both analytical and numerical solutions are presented to predict the instability of this simplified vehicle.

Figure 1 shows the cross section of a vehicle and guideway. Assume that the vehicle is traveling at a constant velocity (v = 36 m/s) along the x direction. Two permanent magnets are attached to the bottom of the vehicle and provide lift and guidance forces F_{L1}, F_{L2}, F_{G1}, and F_{G2}, (see Fig.

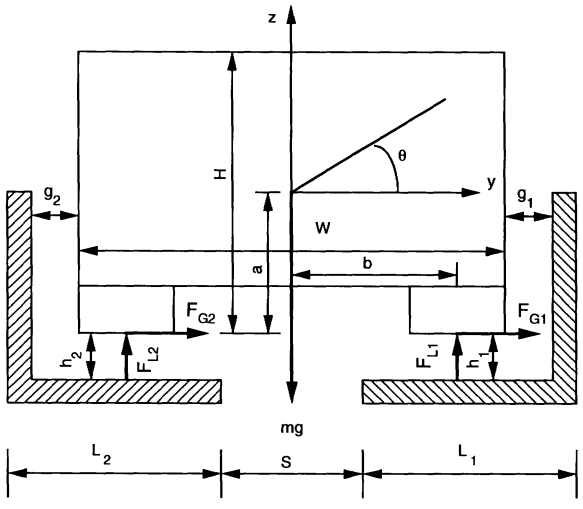

FIGURE 1 Three-DOF maglev system with vehicle operating on double L-shaped aluminum sheet guideway.

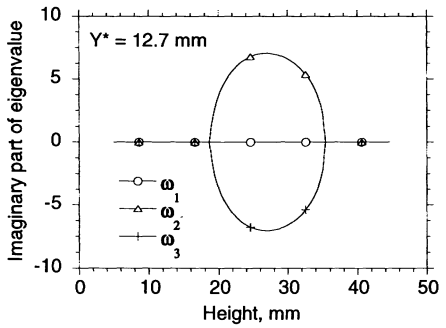

FIGURE 2 Maglev-system eigenvalues vs. vehicle levitation height, with $Y^* = 12.7$ (Cai et al., 1992b).

1). Assuming at the initial state that $h_1 = h_2 = h_0$ and $g_1 = g_2 = g_0$, we can express the geometries of vehicle and guideway as

$$L_1 = L_2 = S = 76.2 \text{ (mm)},$$
$$W = 152.4 + S - 2g_0 \text{ (mm)},$$
$$H = 0.9\,W \text{ (mm)},$$
$$a = 0.5\,H \text{ (mm)},$$
$$b = 0.5(W - 25.4) \text{ (mm)}.$$

The equation of motion for this three-DOF maglev system can be found in Cai et al. (1992a, 1992b). With magnetic forces and motion-dependent magnetic force coefficients measured by the experiments, the eigenvalues and eigenvectors of a maglev vehicle on a double L-shaped guideway were calculated with the analytical model. Figure 2 shows that the imaginary part of the eigenvalues of vehicle motion versus levitation height vary when guidance gaps are fixed ($g_1 = g_2 = Y^* = 12.7$ mm). The second and third modes are coupled slip-roll motions. With a range of height h of 19–35 mm, the imaginary parts of eigenvalues appear not to be zero. This indicates that within this range, flutter exists for these coupled slip-roll vibrations. Figure 3 shows the real part of the eigenvalues of third-mode motion (which presents the transverse motion of a vehicle) versus lateral location of the vehicle when parameter-equilibrium guidance gap varies as $g_1 = g_2 = g_0 = 10$, 15, 20, and 25 mm. We found that divergence appears with the case of $g_0 = 25$ mm, in which the real part of third-mode eigenvalues is zero.

To compare with the analytical solution, as shown in Figs. 2 and 3, a numerical solution was developed with the same vehicle-guideway configuration as in Fig. 1, and experimentally measured magnetic lift and guidance forces were incorporated into the computer code (Nonlinear Dynamic Simulation of Maglev System developed at Argonne). Extensive computations were performed to analyze system parameters and verify the analytical solutions.

Figure 4 shows time histories of heave, slip, and roll motions of a maglev vehicle with zero damping, fixed lateral gap g_0 (=12.7 mm), and two vertical height values $h_0 = 10$ and 25 mm (which correspond to Fig. 2). The slip and roll motions [Fig. 4(b, c)] are apparently stable with $h_0 = 10$ mm, but unstable with $h_0 = 25$ mm, which indicates that coupled slip-roll flutter indeed occurs. These results show very good agreement with the analytical solution in Fig. 2, in which the flutter range exists within a height range of 19–35 mm. Also, divergence of heave motion exists when $h_0 = 25$ mm [Fig. 4(a)]. Figure 5 shows effects of system damping for the three motions with $g_0 = 12.7$ mm and $h_0 = 25$ mm, damping ratio $\zeta = 0.01$, 0.02, 0.05, and 0.10. For $\zeta = 0.01$ and 0.02, the system is still unstable. However, when $\zeta = 0.05$, coupled slip-roll flutter [Fig. 5(b, c)] and divergence of heave motion [Fig. 5(a)] are suppressed by damping and the system becomes stable.

Figure 6 shows time histories of heave, slip, and roll motions with zero damping, fixed vertical height h_0(=7 mm), and two lateral gap values $g_0 = 15$ and 25 mm (which correspond to Fig. 3). Divergence of slip and roll motions occurs when $g_0 = 25$ mm. This not only indicates that the divergence is subjected to lateral vehicle motion as verified in Fig. 3, but also reflects the coupling effects between two motions. Figure 7 shows the effects of system damping for the three motions with $g_0 = 25$ mm and $h_0 = 7$ mm, damping ratio $\zeta = 0.01, 0.02, 0.05$, and 0.10, in which divergence dominates vehicle instability. System damping can suppress flutter but not divergence.

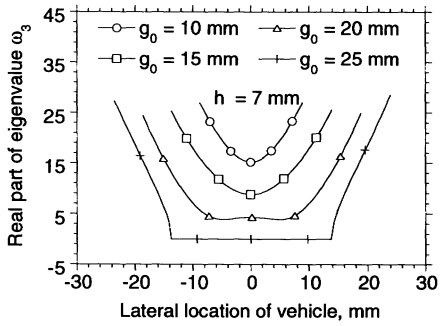

FIGURE 3 Real part of maglev-system eigenvalues vs. lateral location of vehicle, with $h = 7$ mm and $g_0 = 10$, 15, 20, and 25 mm (Cai et al., 1992b).

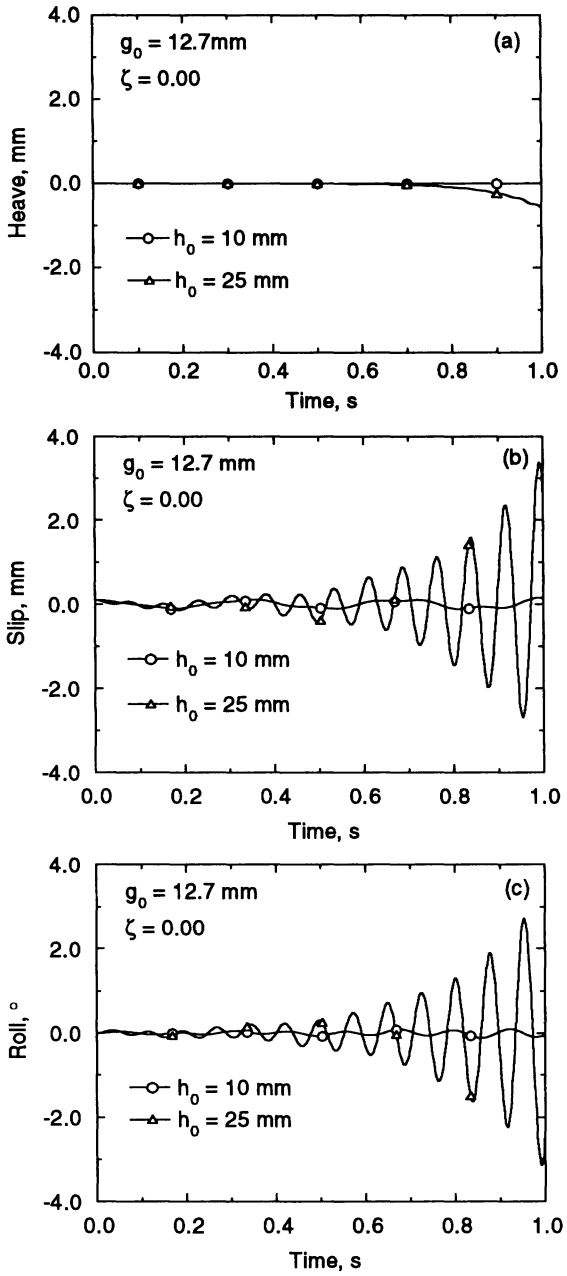

FIGURE 4 Time histories of vehicle motions with various vertical air gaps h_0 when $g_0 = 12.7$ mm, $\zeta = 0.0$.

SIMULATION FOR FIVE-DOF MODEL

When a rigid-body maglev vehicle is levitated over a double L-shaped sheet guideway and is restricted in motion longitudinally, there are five vehicle motions: two translational motions (heave and slip) and three rotational motions (roll pitch, and yaw). Figure 8 schematically shows front and side views of this five-DOF vehicle with four magnets that provide lift force F_L and guidance force F_G over the double L-shaped aluminum sheet guideway. The equilibrium lateral and vertical air gaps between vehicle and guideway are shown by y_0 and z_0, respectively. Assume that magnetic forces provided by the magnets have been determined; therefore, the vertical equilibrium air gap

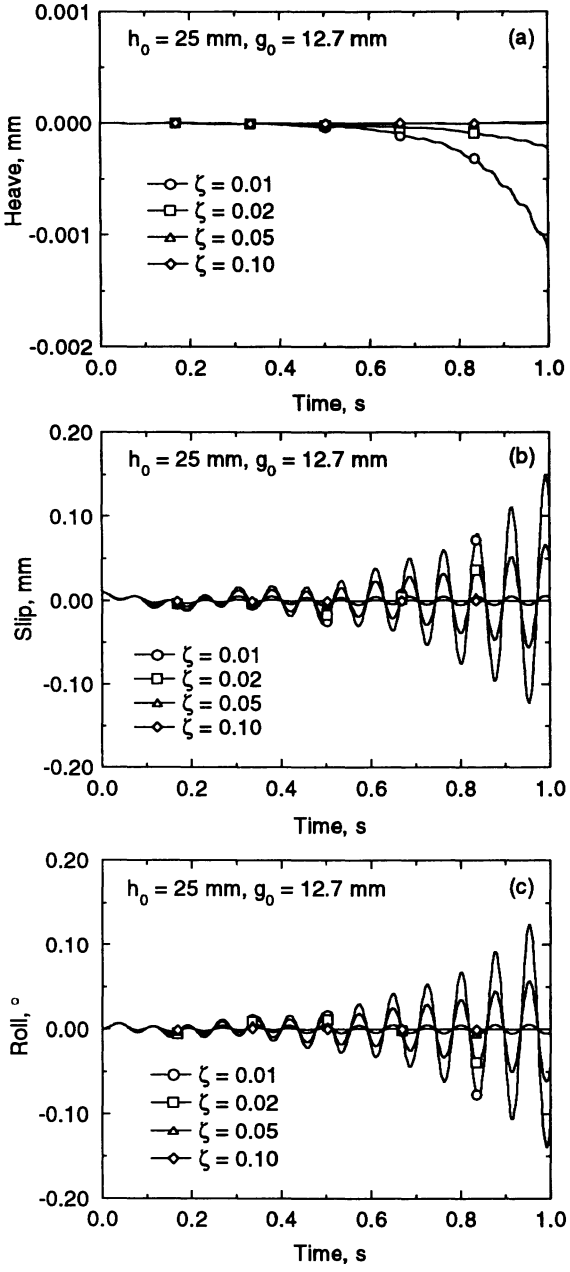

FIGURE 5 Time histories of vehicle motions with various damping coefficients when $h_0 = 25$ mm, $g_0 = 12.7$ mm.

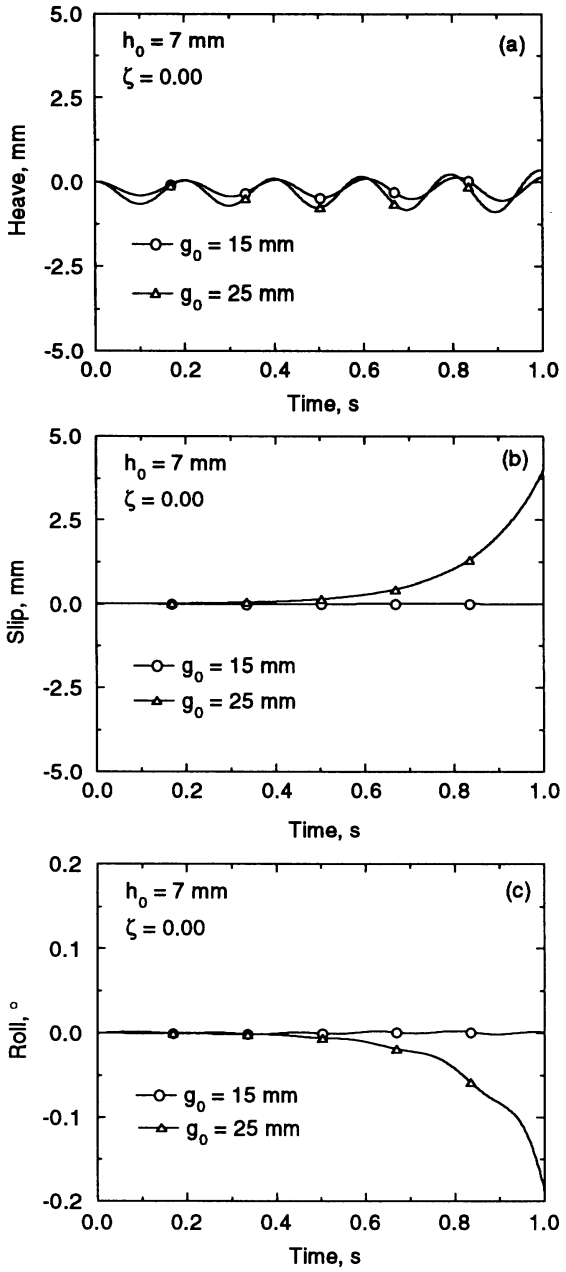

FIGURE 6 Time histories of vehicle motions with various lateral air gaps g_0 when $h_0 = 7$ mm, $\zeta = 0.0$.

is dependent on the vehicle total mass. Distance between center of gravity and magnets is shown by z_c and is dependent on vehicle geometry design. Given the size of magnet as 50.8 × 25.4 × 6.35 mm, the geometry of vehicle and guideway in our simulation is given as

$$L = 2a + 50.8\,(\text{mm}) = 127\,(\text{mm}),$$
$$H = 76.2\,(\text{mm}),$$
$$W = 2b + 25.4 = 2(y_g + y_0 + 25.4)(\text{mm}),$$
$$y_g = 41.275\,(\text{mm}).$$

Governing equations of motion of this five-DOF maglev system are derived from Newton's and Euler's equation, and the transform between vehicle coordinate system and guideway coordinate system is based on Euler angles (Cai et al., 1992b; Coffey et al., 1991).

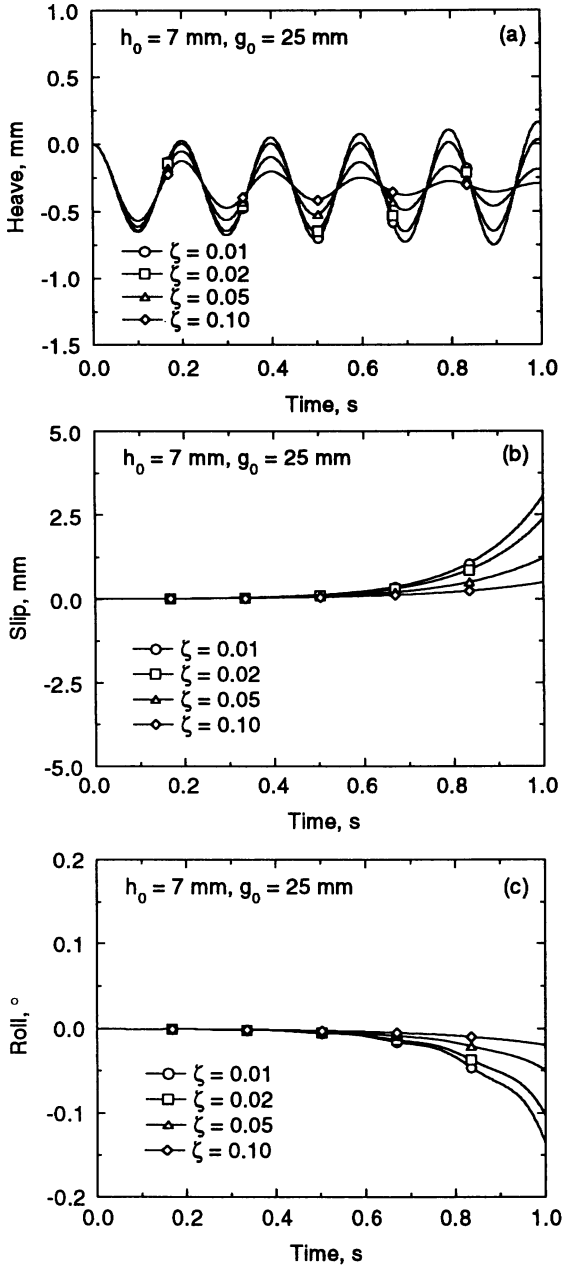

FIGURE 7 Time histories of vehicle motions with various damping coefficients when $h_0 = 7$ mm, $g_0 = 25$ mm.

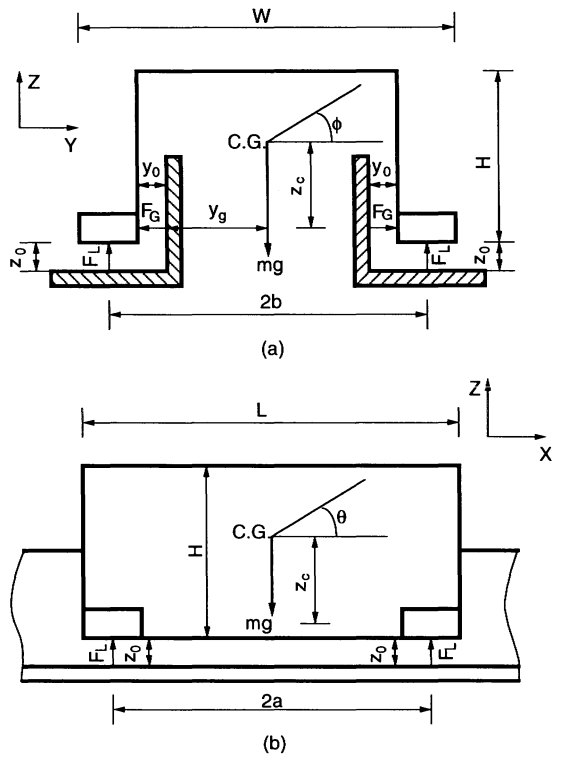

FIGURE 8 Maglev vehicle on double L-shaped aluminum sheet guideway: (a) front view; (b) side view.

Consider a rigid body vehicle with six DOF, three translations, u_x, u_y, u_z, and three rotations, ω_x, ω_y, ω_z (Cai et al., 1992b). Let U be the translation vector and Ω the rotation vector, i.e.,

$$U = \begin{Bmatrix} u_x \\ u_y \\ u_z \end{Bmatrix}, \Omega = \begin{Bmatrix} \omega_x \\ \omega_y \\ \omega_z \end{Bmatrix}. \tag{1}$$

To transform from the vehicle coordinate system to the guideway coordinate system (Coffey et al., 1991), the Euler angles ψ (heading), θ (attack), and ϕ (roll) are introduced. A vector $\mathbf{R}_g$ in the guideway coordinates transforms from a vector $\mathbf{R}_v$ in the vehicle coordinates as

$$\mathbf{R}_g = [l]\mathbf{R}_v \tag{2}$$

with the transformation matrix given by

$$[l] = \begin{bmatrix} \cos\theta\cos\psi & -\sin\psi\cos\phi + \cos\psi\sin\theta\sin\phi & \sin\psi\sin\phi + \cos\psi\sin\theta\cos\phi \\ \cos\theta\sin\psi & \cos\psi\cos\phi + \sin\psi\sin\theta\sin\phi & -\cos\psi\sin\phi + \sin\psi\sin\theta\cos\phi \\ -\sin\theta & \cos\theta\cos\phi & \cos\theta\cos\phi \end{bmatrix}. \tag{3}$$

Equations of motion expressed in the vehicle coordinate system can be described as

$$\left.\begin{aligned} M\ddot{U} + C\dot{U} &= M\mathbf{G} + M(\dot{U} \times \dot{\Omega}) + \mathbf{F}_m \\ I\ddot{U} + D\dot{U} &= I\Gamma + R \cdot \mathbf{F}_m \end{aligned}\right\} \tag{4}$$

where M and I are the mass of the vehicle and the moment of inertia about the center of mass of the vehicle, and are defined by

$$M = \begin{bmatrix} m & 0 & 0 \\ 0 & m & 0 \\ 0 & 0 & m \end{bmatrix}, \mathrm{I} = \begin{bmatrix} I_x & 0 & 0 \\ 0 & I_y & 0 \\ 0 & 0 & I_z \end{bmatrix}. \tag{5}$$

C and D are damping coefficients matrices

$$C = \begin{bmatrix} c_{11} & c_{12} & c_{13} \\ c_{21} & c_{22} & c_{23} \\ c_{31} & c_{32} & c_{33} \end{bmatrix}, \quad D = \begin{bmatrix} d_{11} & d_{12} & d_{13} \\ d_{21} & d_{22} & d_{23} \\ d_{31} & d_{32} & d_{33} \end{bmatrix}. \tag{6}$$

The damping coefficient in Eq. (6) should be determined from experimental data. Before these experimental data are available, assumed damping ratios can be utilized in the simulations. The elements of $\mathbf{G}$ and Γ are defined by

$$\mathbf{G} = \begin{Bmatrix} -g\sin\theta \\ g\cos\theta\sin\phi \\ g\cos\theta\cos\phi \end{Bmatrix} \tag{7}$$

and

$$\Gamma = \begin{Bmatrix} \dfrac{I_y - I_z}{I_x}\dot{\omega}_y\dot{\omega}_z \\ \dfrac{I_z - I_x}{I_y}\dot{\omega}_z\dot{\omega}_x \\ \dfrac{I_x - I_y}{I_z}\dot{\omega}_w\dot{\omega}_y \end{Bmatrix}. \tag{8}$$

$\mathbf{F}_m$ is magnetic force applied on the center of mass. R is moment arm matrix. Because the applied forces depend on the distances between the vehicle and the guideway surfaces, but all components of the forces and moments in the equations of motion are to be expressed along the axes of the vehicle, the transformation is required to convert forces from one coordinate to the other.

The time derivatives of the Euler angles ψ, θ, and ϕ are related to the rotational velocities, thus

$$\left.\begin{aligned} \dot{\psi} &= \sec\theta(\dot{\omega}_z \cos\phi + \dot{\omega}_y \sin\phi) \\ \dot{\theta} &= \dot{\omega}_y \cos\phi - \dot{\omega}_z \sin\phi \\ \dot{\phi} &= \dot{\omega}_x + \tan\theta(\dot{\omega}_z \cos\phi + \dot{\omega}_y \sin\phi) \end{aligned}\right\} \quad (9)$$

Because only a five-DOF vehicle model is considered in the dynamic simulation and experiments with the Argonne rotating-wheel facility,

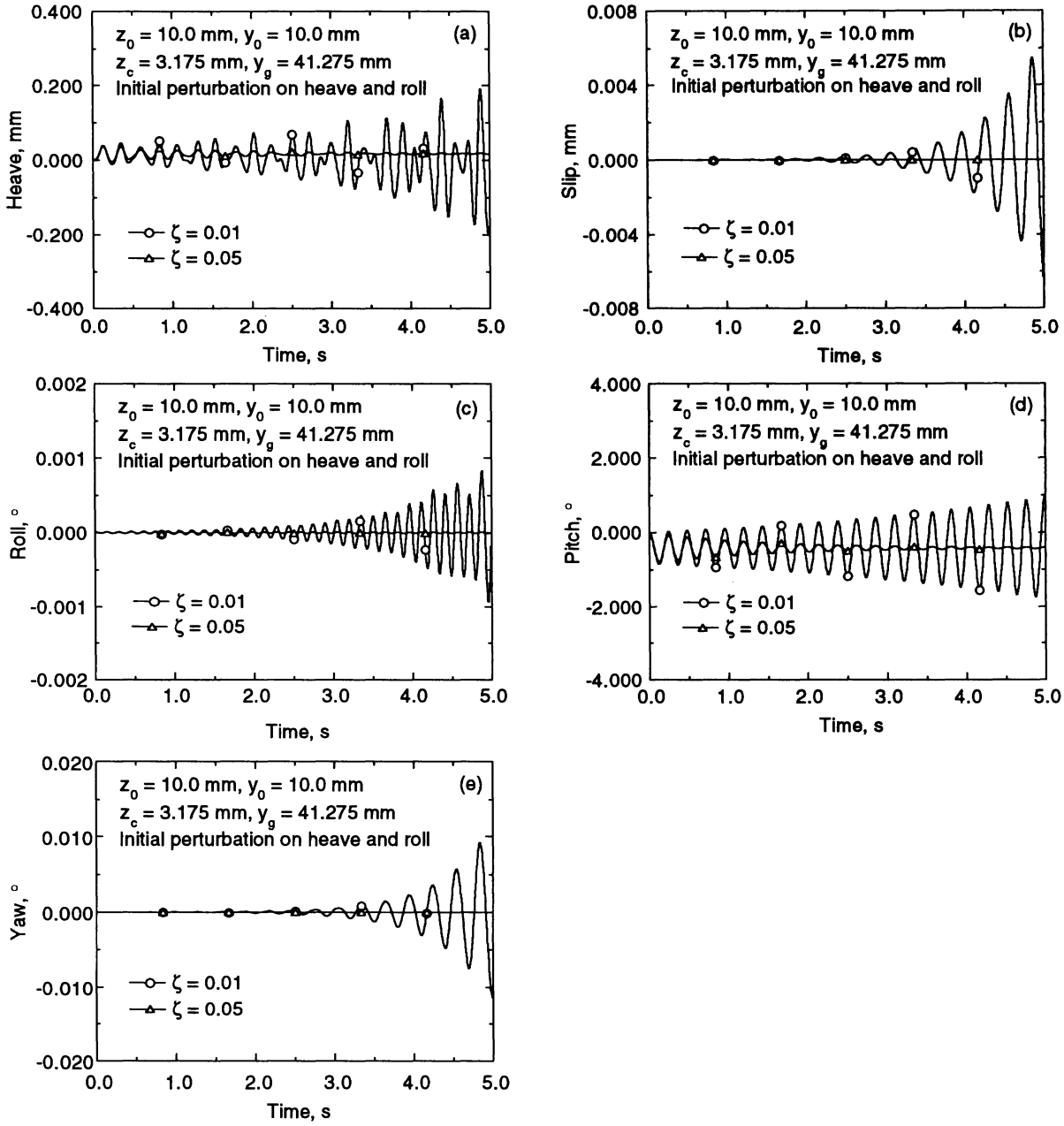

FIGURE 9 Time histories of vehicle motions perturbed on heave and roll directions at various damping coefficients.

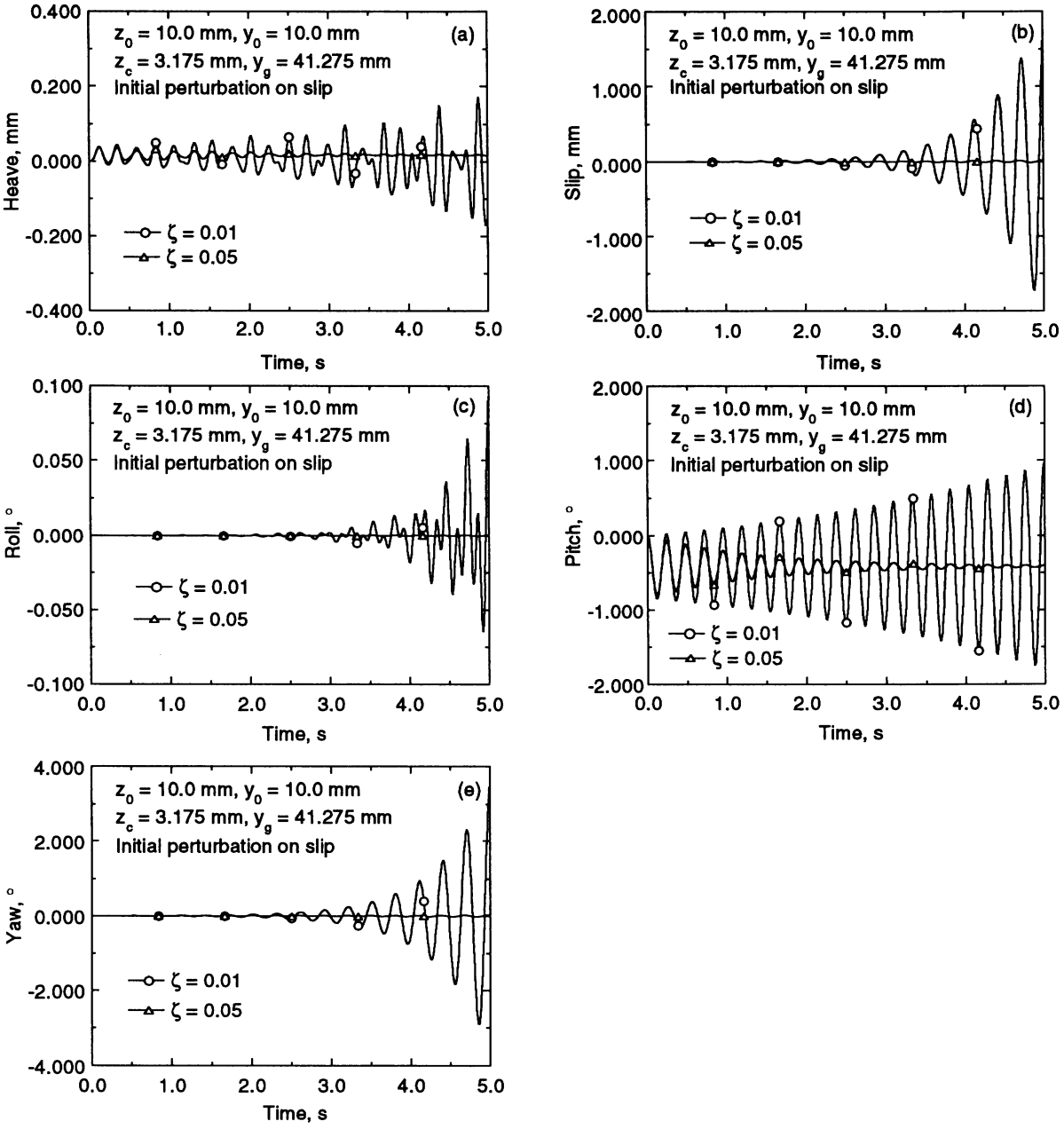

FIGURE 10 Time histories of vehicle motions perturbed on slip direction at various damping coefficients.

the longitudinal motion of the vehicle u_x is restricted and can be assumed to be zero in the equations of motion.

Based on governing equations, Eqs. (4)–(9), a computer code for a five-DOF maglev system was written. Magnetic force data from experimental measurements are included in force subroutines of the code. This code can numerically integrate nonlinear differential equations using the fourth-order Runge–Kutta method.

Figures 9 and 10 show time histories of five motions with z_0 = 10 mm, y_0 = 10 mm, and z_c = 3.175 mm and at system damping ratios ζ = 0.01 and 0.05 when given initial perturbation on heave and roll motions (Fig. 9) and slip motion (Fig. 10), respectively. When ζ = 0.01, the system appears unstable, or flutter occurs in all five motions, no matter which directions is initially perturbed. When system damping increases to 0.05, the system becomes stable.

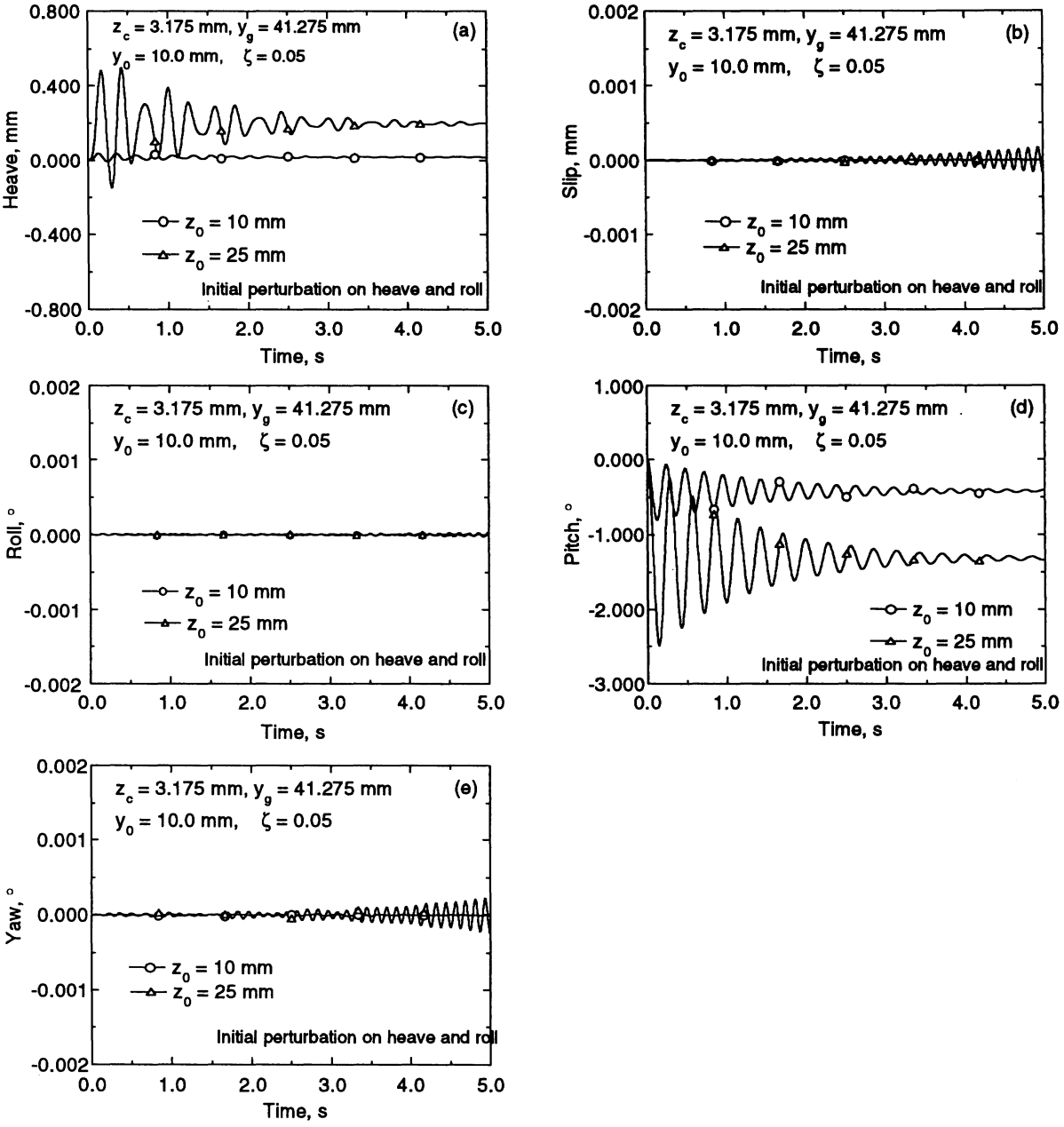

FIGURE 11 Time histories of vehicle motions with various vertical air gaps when $\zeta = 0.05$.

Figure 11 shows the difference when applying initial equilibrium vertical air gap, $z_0 = 10$ mm and $z_0 = 25$ mm; this reflects the effect of vehicle mass (lateral gap remains the same, $y_0 = 10$ mm). Even with $\zeta = 0.05$, flutters exist with slip and yaw motions when the air gap $z_0 = 25$ mm. To some degree, this is consistent with the results from the three-DOF vehicle model (see Figs. 2 and 4) because we used the same magnetic force data in our simulations.

In Figure 12, the center of gravity is changed to $z_c = 0.0$ mm. In this case, with $\zeta = 0.01$, heave perturbation causes flutter only in heave motion [Fig. 12(a)], and roll perturbation causes flutter only in roll motion [Fig. 12(c)]. Slip perturbation causes flutter in both slip and yaw motions [(Fig. 12(b,e)], while in Figs. 9 and 10, one-direction perturbation can cause instabilities in several motions. We can even find the frequency of coupled motion [Figs. 9(a), 10(a), and 10(c)]. It can be

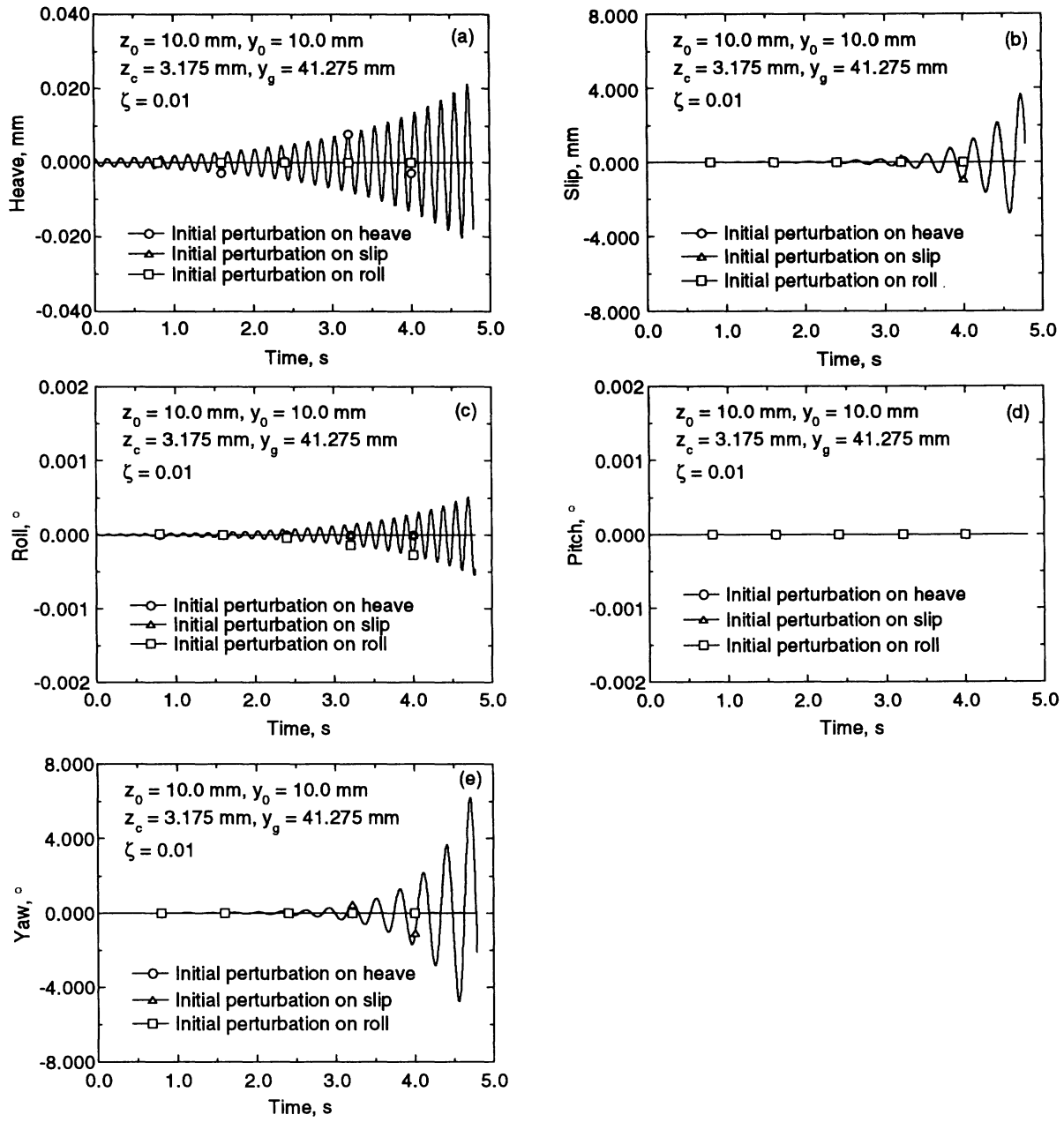

FIGURE 12 Time histories of vehicle motions when $z_0 = 0.0$ and perturbed on different directions.

concluded that vehicle geometry will introduce not only instability, but also coupling effects in maglev designs.

CONCLUSIONS

In this study, we have theoretically investigated the instability of an electrodynamic maglev system with three- and five-DOF vehicles traveling on a double L-shaped set of guideway conductors, using steady magnetic forces and motion-dependent magnetic force coefficients. For the three-DOF maglev system, flutter and divergence instabilities were predicted from both analytical and numerical solutions; these instabilities depend on the initial equilibrium air gap, which is determined by vehicle mass and vehicle/guideway geometry design. For the five-DOF maglev system, lengthy parameter analyses must be performed, and instabilities of five direction motions (heave, slip, roll, pitch, and yaw) of the dynamic

vehicle model are observed. System parameters, such as damping, vehicle mass, vehicle/guideway geometry, and coupling effects among five diffferent motions, play very important roles in determining the dynamic instabilities of maglev vehicles.

This work was performed under the sponsorship of the US Army Corps of Engineers and the Federal Railroad Administration, through interagency agreements with the US Department of Energy.

REFERENCES

Cai, Y., Chen, S. S., Mulcahy, T. M., and Rote, D. M., 1992a, "Dynamic Stability of Maglev Systems," *Proceedings of the 63rd Shock and Vibration Symposium,* October 27–29, 1992, Las Cruces, NM, pp. 533–543.

Cai, Y., Chen, S. S., Mulcahy, T. M., and Rote, D. M., 1992b, "Dynamic Stability of Maglev Systems," Report ANL-92/21, Argonne National Laboratory, Argonne, IL.

Cai, Y., Chen, S. S., Zhu, S., Mulcahy, T. M., Rote, D. M., and Coffey, H. T., 1993a, "Dynamics, Stability, and Control of Maglev Systems," *Proceedings of Maglev '93, 13th International Conference on Magnetically Levitated Systems and Linear Drives,* May 19–21, 1993, Argonne, IL, pp. 265–270.

Cai, Y., Zhu, S., Chen S. S., and Rote, D. M., 1993b, "Control of Maglev Suspension Systems," 1993 ASME Pressure Vessels and Piping Conference, July 25–29, 1993, Denver, CO, ASME Publication, PVP-Vol. 256-2, pp. 57–67.

Chu, D., and Moon, F. C., 1983, "Dynamic Instabilities in Magnetically Levitated Models," *Journal of Applied Physics,* Vol. 54, pp. 1619–1625.

Coffey, H. T., He, J. L., Chang, S. L., 1991, "Preliminary Design for a Maglev Development Facility," Report AN:/ESD-14, Argonne National Laboratory, Argonne, IL.

Davis, L. C., and Wilkie, D. F., 1971, "Analysis of Motion of Magnetic Levitation Systems: Implications," *Journal of Applied Physics,* Vol. 42, pp. 4779–4793.

Moon, F. C., 1974, "Laboratory Studies of Magnetic Levitation in the Thin Track Limit," *IEEE Transactions on Magnetics,* MAG-10, No. 3, pp. 439–442.

Moon, F. C., "Vibration Problems in Magnetic Levitation and Propulsion," in E. R. Laithwaite, *Transport Without Wheels,* Elek Science, London, pp. 122–161.

Ohno, E., Iwamoto, M., and Yamada, T., 1973, "Characteristic of Superconductive Magnetic Suspension and Propulsion for High-Speed Trains," *Proceedings IEEE,* Vol. 61, pp. 579–586.